The ICECUBE prototype string in AMANDA

The AMANDA Collaboration

M. Ackermann [d], J. Ahrens [k], X. Bai [a], M. Bartelt [t], S.W. Barwick [j], R. Bay [i], T. Becka [k], J.K. Becker [t], K.-H. Becker [b], E. Bernardini [d], D. Bertrand [c], D.J. Boersma [d], S. Böser [d], O. Botner [q], A. Bouchta [q], O. Bouhali [c], J. Braun [o] C. Burgess [r], T. Burgess [r], T. Castermans [m], W. Chinowsky [g], D. Chirkin [g], J. Conrad [q], J. Cooley [o], D.F. Cowen [h], A. Davour [q], C. De Clercq [s], T. DeYoung [ℓ], P. Desiati [o], P. Ekström [r], T. Feser [k], M. Gaug [d], T.K. Gaisser [a], R. Ganugapati [o], H. Geenen [b], L. Gerhardt [j], A. Goldschmidt [g], A. Groß [t], A. Hallgren [q], F. Halzen [o], K. Hanson [o], R. Hardtke [i], T. Harenberg [b], T. Hauschildt [a], K. Helbing [b,*], M. Hellwig [k], P. Herquet [m], G.C. Hill [o], D. Hubert [s], B. Hughey [o], P.O. Hulth [r], K. Hultqvist [r], S. Hundertmark [r], J. Jacobsen [g], K.H. Kampert [b], A. Karle [o], J.L. Kelley [o], M. Kestel [h], G. Kohnen [m], L. Köpke [k], M. Kowalski [d], M. Krasberg [o], K. Kuehn [j], H. Leich [d], M. Leuthold [d], I. Liubarsky [e], J. Ludvig [g,1], J. Lundberg [q], J. Madsen [p], P. Marciniewski [q], H.S. Matis [g], C.P. McParland [g], T. Messarius [t], Y. Minaeva [r], P. Miočinović [i], R. Morse [o], K.S. Münich [t], R. Nahnhauer [d], J. Nam [j], T. Neunhöffer [k], P. Niessen [a], D.R. Nygren [g], H. Ögelman [o], Ph. Olbrechts [s], C. Pérez de los Heros [q], A.C. Pohl [f], R. Porrata [i], P.B. Price [i], G.T. Przybylski [g], K. Rawlins [o], E. Resconi [d], W. Rhode [t], M. Ribordy [m], S. Richter [o], S. Robbins [b], J. Rodríguez Martino [r], H.-G. Sander [k], S. Schlenstedt [d], D. Schneider [o], R. Schwarz [o], A. Silvestri [j], M. Solarz [i], J. Sopher [g] G.M. Spiczak [p], C. Spiering [d], M. Stamatikos [o], D. Steele [o], P. Steffen [d], R.G. Stokstad [g], K.-H. Sulanke [d], I. Taboada [n] L. Thollander [r], S. Tilav [a], W. Wagner [t], C. Walck [r], M. Walter [d], Y.-R. Wang [o], C. Wendt [o], C.H. Wiebusch [b], R. Wischnewski [d], H. Wissing [d], K. Woschnagg [i], G. Yodh [j]

[a]*Bartol Research Institute, University of Delaware, Newark, DE 19716, USA*

[b]*Fachbereich C – Physik, BU Wuppertal, D-42119 Wuppertal, Germany*

[c]*Université Libre de Bruxelles, Science Faculty, Brussels, Belgium*

[d]*DESY-Zeuthen, D-15738 Zeuthen, Germany*

[e]*Blackett Laboratory, Imperial College, London SW7 2BW, UK*

[f]*Dept. of Chemistry and Biomedical Sciences, University of Kalmar, S-39182 Kalmar, Sweden*

[g]*Lawrence Berkeley National Laboratory, Berkeley, CA 94720, USA*

[h]*Dept. of Physics, Pennsylvania State University, University Park, PA 16802, USA*

[i]*Dept. of Physics, University of California, Berkeley, CA 94720, USA*

[j]*Dept. of Physics and Astronomy, Univ. of California, Irvine, CA 92697, USA*

[k]*Institute of Physics, University of Mainz, D-55099 Mainz, Germany*

[ℓ]*Dept. of Physics, University of Maryland, College Park, MD 20742, USA*

[m]*University of Mons-Hainaut, 7000 Mons, Belgium*

[n]*Dept. de Física, Universidad Simón Bolívar, Caracas, 1080, Venezuela*

[o]*Dept. of Physics, University of Wisconsin, Madison, WI 53706, USA*

[p]*Physics Dept., University of Wisconsin, River Falls, WI 54022, USA*

[q]*Div. of High Energy Physics, Uppsala University, S-75121 Uppsala, Sweden*

[r]*Dept. of Physics, Stockholm University, SE-10691 Stockholm, Sweden*

[s]*Vrije Universiteit Brussel, Dienst ELEM, B-1050 Brussels, Belgium*

[t]*Institute of Physics, University of Dortmund, D-44221 Dortmund, Germany*

Abstract

The **A**ntarctic **M**uon **A**nd **N**eutrino **D**etector **A**rray (AMANDA) is a high-energy neutrino telescope. It is a lattice of optical modules (OM) installed in the clear ice below the South Pole Station. Each OM contains a photomultiplier tube (PMT) that detects photons of Cherenkov light generated in the ice by muons and electrons. ICECUBE is a cubic-kilometer-sized expansion of AMANDA currently being built at the South Pole. In ICE-CUBE the PMT signals are digitized already in the optical modules and transmitted to the surface. A prototype string of 41 OMs equipped with this new all-digital technology was deployed in the AMANDA array in the year 2000. In this paper we describe the technology and demonstrate that this string serves as a proof of concept for the ICECUBE array. Our investigations show that the OM timing accuracy is 5 ns. Atmospheric muons are detected in excellent agreement with expectations with respect to both angular distribution and absolute rate.

* Corresponding author: Klaus Helbing. Address: Fachbereich C – Physik, Gaußstr. 20, Bergische Universität Wuppertal , D-42119 Wuppertal, Germany; Phone: +49 202 439 2829 Fax: +49 202 439 2662
    Email address:
helbing@uni-wuppertal.de (K. Helbing).
[1] now at Stanford Research Systems, Sun-

1 Introduction

The **A**ntarctic **M**uon **A**nd **N**eutrino **D**etector **A**rray (AMANDA) [1] at the geographic South Pole is a lattice of

nyvale, CA 94089, USA

photomultiplier tubes (PMTs) each enclosed in a transparent pressure sphere to comprise an optical module (OM). The OMs are buried in the polar ice at depths between 1500 m and 2000 m. The primary goal of AMANDA is to discover astrophysical sources of high energy neutrinos. High-energy muon neutrinos penetrating the earth from the Northern Hemisphere are identified by the secondary muons produced in charged current neutrino-nucleon interactions near or within the detector. AMANDA was the first neutrino telescope with an effective area in excess of 10000 m^2 – with over 600 optical modules in place.

Large as it is, AMANDA is only capable of seeing the brighter (and closer) sources of neutrinos. ICECUBE will be an array of 4,800 optical modules within a cubic kilometer of ice [2]. Frozen into vertical holes 2.4 km deep, drilled by hot water, the optical modules will lie between 1450 m and 2450 m below the surface. An instrument of this size is suited to study neutrinos from distant astrophysical sources [3].

The optical modules in AMANDA and ICECUBE are arranged like strings of beads connected electrically and mechanically to long cables leading up to a control room at the surface. The PMT within the OM detects individual photons of Cherenkov light generated in the ice by muons and electrons moving with velocities near the speed of light. Signal events consist primarily of up-going muons produced in neutrino interactions in the bedrock of Antarctica or in the ice. In addition, the detector will identify electromagnetic

and hadronic showers ("cascades") from interactions of ν_e and ν_τ inside the detector volume provided they are sufficiently energetic. Background events are mainly downward-going muons from cosmic ray interactions in the atmosphere above the detector. For ICECUBE, the background will be monitored for calibration purposes by the ICETOP air shower array [2] covering a 1 km^2 area at the ice surface right above the in-ice OMs of the ICECUBE detector. This background will also be used as a test beam for commissioning the detector.

Unlike AMANDA, ICECUBE PMT signals are digitized directly in the optical module itself and then transmitted digitally to the surface. This is done such that the arrival time of a photon at an OM can be determined to within a few nanoseconds. The electronics at the surface determines when an event has occurred (e.g., that a muon traversed or passed near the array) and records the information for subsequent event reconstruction and analysis.

In the following we will discuss the performance obtained with a string of 41 Digital Optical Module (DOM) prototypes 12 m apart deployed in January 2000 by the AMANDA Collaboration as the 18th string (STRING-18) of the AMANDA array.

2 Digital technology

The DOMs of STRING-18 were intended to demonstrate the advantages and the feasibility of a purely digital technical approach, in which PMT sig-

nals are captured and digitized locally, within the optical module. The digital data are transmitted to the surface using the twisted pair copper conductors that also bring power and control signals to the DOMs. We will discuss the design, data taking and data analysis of STRING-18.

2.1 Concept

Very large high-energy cosmic neutrino detectors require photomultiplier tubes to be located far from the signal processing center. The completed AMANDA detector represents an evolution of signal transmission technologies from coaxial cable to twisted copper pair to optical fiber. In all these cases, the analog signals are brought to the surface, where they are digitized and processed.

The longer cable lengths, the much larger number of PMTs of ICECUBE and the requirements of a larger dynamic range for PMT pulses and improved time resolution, as compared to AMANDA, have led to the development of a data-acquisition technology with the following features:

(1) Robust copper cable and connectors between the surface and the modules at depth.
(2) Digitization and time-stamping of signals that are unattenuated and undispersed.
(3) Calibration methods (particularly for timing) that are appropriate for a very large number of optical modules.

The PMT anode signal is digitized and time-stamped already in the optical module. Waveform digitization, in which all the information in a PMT anode signal is captured, is incorporated. The time calibration procedure is both accurate and automatic.

There are three fundamental elements to the data acquisition architecture of ICECUBE and STRING-18:

- The Digital Optical Module (DOM), which captures the signals induced by physical processes and preserves the information quality through immediate conversion to a digital format using an innovative ASIC, the Analog Transient Waveform Digitizer (ATWD [4], see Sec. 2.2.4.1).
- A Network, which connects the highly dispersed array of optical modules to the surface data acquisition system (DAQ) and provides power to them.
- A Surface DAQ, which maintains a master clock time-base and provides all messaging, data flow, filtering, monitoring, calibration, and control functions.

2.2 Digital optical module (DOM)

The basic elements of the DOM are the PMT for detection of Cherenkov light, a printed circuit board (PCB) for processing signals, a HV generator for the PMT, and an optical beacon consisting of LEDs for calibration purposes all within the glass pressure housing. The general physical layout of a DOM is shown in Fig. 1.
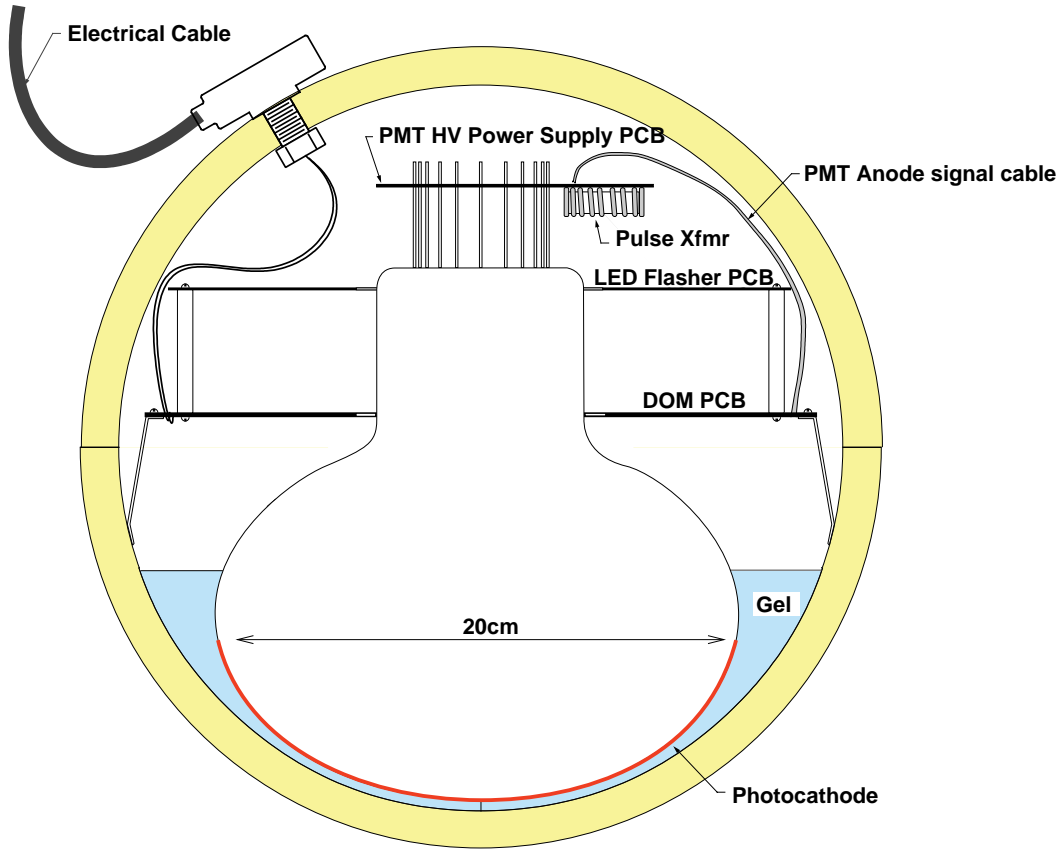
Figure 1. Schematic profile view of a STRING-18 Digital Optical Module, showing pressure sphere, optical coupling gel, photomultiplier, digital signal processing board (DOM PCB), LED flasher board, PMT base, and electrical penetrator.

2.2.1 Pressure Housing

The spherical glass pressure housings are standard items used in numerous oceanographic and maritime applications. The most important qualities are mechanical reliability, cost, optical transmission, low radioactivity, and low scintillation of the glass. For STRING-18 "Benthospheres" are used, a trade-name of Benthos, Inc.

2.2.2 Photomultiplier

The optical sensor of the DOM is a large (8 inch diameter) hemispherical 14-stage photomultiplier tube, the Hamamatsu R5912-02 with a gain of $4 \cdot 10^8$ at the typical operational voltage of 1400 V. These large PMTs offer good time-resolution, as indicated by a transit-time-spread (TTS) for single photoelectron pulses of about 2.5 ns rms. Despite their large photocathode area, these PMTs alone [2] generate only 300 Hz or less of dark noise pulses at temperatures below freezing and 1400 V. The photocathode sensitivity extends well into the UV. The reception of Cherenkov photons is limited by the optical transmission of the glass pressure sphere at 350 nm. The PMT

---

[2] The dominant source of noise of the integrated OM is the glass of the pressure sphere which leads to a total of about 1 kHz noise pulse rate.
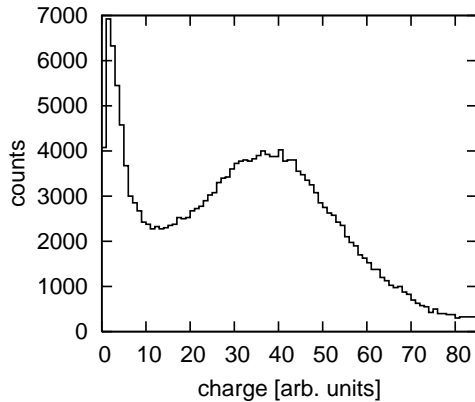
Figure 2. Measured integral charge distribution of DOM #1. Most of the histogram is single photoelectron noise pulses.

HV generator is a multi-stage voltage multiplier with an oscillator running at a few tens of kHz. It converts the electrical power transmitted via copper cable down into the ice to a high voltage for the PMT.

For each photon that produces a single photoelectron, the PMT produces pulses that have characteristic rise (fall) times of 7 (11) ns. Due to the stochastic nature of the PMT's electron multiplication process, single photoelectron pulses display significant variations in pulse shape and amplitude. The measured integrated charge distribution of the deepest DOM (DOM #1) is shown in Fig. 2. The peak to valley ratio is very good for an 8 inch photomultiplier.

2.2.3   Optical beacon

Each of the STRING-18 DOMs is equipped with 6 GaN LEDs, which emit predominantly in the near-UV at 370 nm. The luminous intensity and the pulsing rate may be varied over a wide range under software control. At their brightest, these beacons can be seen by OMs up to distances of 200 m. The pulse width is 5 ns. The LEDs are broad angular emitters, spaced at 60° around a vertical axis, and are canted over by 45° to produce a roughly hemispherical source.

2.2.4   Signal processing circuitry

Fig. 3 shows the principal components of the Digital Optical Module signal processing circuitry: the analog transient waveform digitizer (ATWD), a low-power custom integrated circuit that captures the waveform in 128 samples at a rate [3] of ~ 600 MHz; a fast ADC operating at [3] ~ 30 MHz covering several microseconds; a FPGA that provides state control, time stamps events, handles communications, etc.; a low-power 32-bit ARM CPU with a real-time operating system. A very stable ($\delta f / f \sim 5 \cdot 10^{-11}$ over ~ 5 s) Toyocom 16.8 MHz oscillator is used to provide clock signals to several components. Short cables connecting adjacent DOM modules enable a local time coincidence (see Sec. 2.3.1), which eliminates most of the ~ 1 kHz of noise pulses when enabled.

The DOM is operated as a slave to the surface DAQ. Upon power-up, it enters a wait state for an interval of a few seconds, to permit downloading of new firmware or software. If no messages are received before time-out, the DOM will boot from Flash memory and await commands.

Normal operation of the DOM is

---

[3]   The sampling speeds in ICECUBE are different from those chosen for STRING-18.
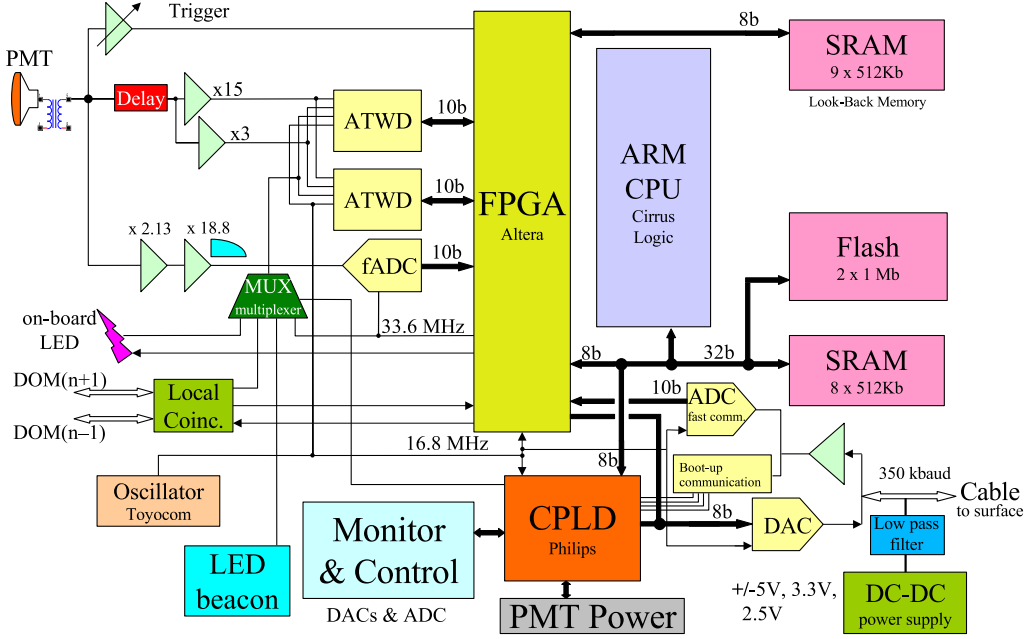
Figure 3. Block diagram of the digital optical module signal processing circuitry.

dominated by a data-taking state (see Sec. 2.2.4.1). In addition, a local-time calibration process is periodically invoked, so that the local DOM time may be ultimately transformed to master clock time with nanosecond accuracy (see Sec. 3). The time calibration process appears as a separately scheduled thread, with no deleterious impact upon the data-taking state. Other active threads are message receive/send and data transmission, also invisible to the data-taking process. There are several calibration modes, such as running optical beacons, during which normal data-taking of the respective DOM is inactive.

Low power consumption was a high priority for the development of the DOM circuitry because electrical power is limited at the South Pole.

Each STRING-18 prototype DOM uses only 3.5 W when booted up and transmitting data. An important feature in this respect is the power consumption specific to the PMT pulse capture process since electronic devices operated at high frequencies usually impose significant demands.

2.2.4.1 PMT pulse capture The DOM is equipped with innovative circuitry that is well-matched to the PMT pulse characteristics and dynamic range. The DOM concept takes advantage of the fact that, most of the time, no PMT pulses are present: The average time between pulses is about 2 ms. Circuit activity need occur only when pulses appear. The waveform (pulse shape) capture capability is realized through a custom switched capacitor

7

array based Application Specific Integrated Circuit (ASIC) designed at Lawrence Berkeley National Laboratory (LBNL), the Analog Transient Waveform Digitizer (ATWD) [4]. The DOM has two such ATWDs with identical tasks for fast switching from one digitizing ATWD to the other ATWD. This minimizes the dead time due to the digitization process.

The ATWD has four channels, each with 128 samples, that synchronously record different input waveforms. Its employment in the DOM is particularly advantageous because its power consumption is only 200 mW. The ATWD performance combination of up to a GHz sampling speed with very low power dissipation is unmatched by any single commercial device for waveform capture. The DOM prototypes in STRING-18 are equipped with a $15\times$ and a $3\times$ gain channel (see Fig. 3). The third channel is routed to an analog multiplexer (MUX) that can connect to various internal signals for diagnostic purposes. The fourth ATWD channel in STRING-18 DOMs is permanently connected to the DOM internal clock, for calibration and monitoring of the ATWD sampling speed.

The upper limit of linearity in pulse height for the lower gain channel of the ATWD was found to be about 150 photoelectrons for a single pulse. This was achieved without extensive optimization of PMT voltages and threshold.

The waveform capture process is initiated by a "launch" signal derived from a discriminator connected to the signal path. The capture process stores waveform samples as analog voltages on
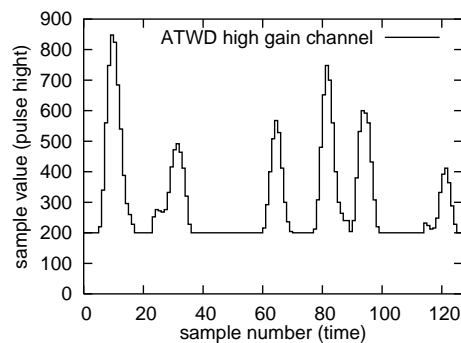

Figure 4. Waveform likely caused by a down-going muon recorded in the DOM closest to a reconstructed track.

four internal linear capacitor arrays. A single DC current applied to the ATWD controls the sampling speed. For STRING-18 we have chosen to capture the pulse shape at 600 MHz (1.7 ns/sample). This high speed capture is useful for characterizing PMT signal shape with good resolution and for other diagnostic purposes. All four channels within an ATWD are sampled syncronously, with aperture variations between channels measured to be less than 10 ps. Fig. 4 shows a particularly feature-rich example of a waveform as recorded by an ATWD with its high-gain channel. The data were obtained with zero suppression and data compression (see Sec. 2.3) in place. Due to the zero suppression all values below the threshold of 200 [4] are represented as the threshold value. The muon track reconstruction discussed later in Sec. 5.2 indicates that the PMT signal was caused by a down going muon with this DOM being the closest to the muon track. This plot demonstrates the capability of separating individual pulses and other details

[4] corresponding to a quarter of the average single photoelectron amplitude with respect to a baseline level of 100.

within the ATWD waveform. Recording the full structure of waveforms will aid in reconstructing complex events.

For waveforms that exceed the ATWD capture interval, sampling at a lower frequency is sufficient to capture relevant information at later times. For this purpose, the DOM is equipped with a 10-bit low-power fADC[5], operating at the DOM local clock frequency of 33.6 MHz. The PMT signal in this path is stretched to match the lower sampling rate.

2.2.4.2 Local time Each PMT hit must be time-stamped such that correlated hits throughout the detector meet the relative timing accuracy requirement of 5 ns rms. This is accomplished within the DOM using a two-stage method that produces a coarse time-stamp and a fine time-stamp. The STRING-18 DOM FPGA maintains a 54-bit local clock running at the DOM 33.6 MHz clock frequency. Once data reach the surface, the local time units as defined by the local clock reference are transformed to master clock units, and are ultimately linked to GPS (see Sec. 3). The 33.6 MHz is obtained by frequency-doubling the free-running Toyocom 16.8 MHz quartz oscillator.

The PMT signal triggers a discriminator. The discriminator pulse is then resynchronized to the next DOM clock transition edge providing the coarse time-stamp. At 33.6 MHz, this coarse time-stamp has a time quantization of 29.8 ns. The resynchronized pulse of

the discriminator provides the ATWD "launch" signal. The synchronous launching causes the PMT signal to arrive within a one-clock-cycle wide time window at the ATWD. The leading edge[6] of the PMT signal waveform within the ATWD record will occur somewhere within this particular 29.8 ns interval. This is the "fine time-stamp" which provides the desired time resolution of less than 5 ns.

For this to work, the PMT signal must be delayed sufficiently such that the leading edge of the signal always appears well after the ATWD sampling action has begun. An overall delay of about 75 ns is needed to accommodate both the coarse time-stamp random delay and the propagation delay of the trigger processing path the circuitry. In the STRING-18 DOM prototypes, a coil of coaxial cable of 15 m length was employed for this purpose.

2.3 Network: Data link to the surface

All timing calibration, control, and communications signals between a given DOM and the surface DAQ are provided by one conventional twisted pair of 0.9 mm diameter copper conductors. This pair also supplies power to the DOM. The resulting cable link is both cost-effective and robust, since the number of connections needed for all functionality is minimal. The twisted pairs are assembled first in double pairs, as "twisted quads", and

---

[5] This fADC is a fast, 10-bit, parallel-output, pipeline ADC

[6] More sophisticated methods than the leading edge to determine the fine time-stamp can be easily envisaged.

enclosed in a common sheath. The required number of twisted quads per string are then wrapped around a Kevlar strength member and covered with a protective sleeve. Breakouts of individual quads to facilitate connections to the DOMs are introduced at the appropriate positions.

The gross bandwidth across this 2.5 km long copper cable reached in STRING-18 was about 35 kilobytes/s. With two ATWD waveform channels of 128 10-bit sample values each and an fADC of 256 10-bit samples the data size of a hit is 640 bytes not accounting for overhead. The hit rate in STRING-18 is about 500 Hz while the single pulse rate is about 1 kHz. [7] The resulting data rate is in excess of 300 kB/s which clearly exceeds the available bandwidth.

We have developed two methods to reduce the amount of data to be transfered from the DOM to the surface: local coincidence and data compression.

2.3.1 Local coincidence

The DOM noise rate is approximately 100 times greater than the rate induced by high-energy muons. Unlike hits due to high energy particles, noise hits in one DOM occur uncorrelated with hits

of neighboring DOMs, i.e. primarily as geometrically isolated hits. A local coincidence requirement, imposed in the ice, selects predominantly only interesting hits for transmission to the surface. Each DOM communicates with its nearest neighbors by means of a dedicated short copper wire pair. The DOM is capable of sending and receiving these short signals in a full duplex mode across these wires. Once a DOM has triggered an ATWD, it sends signals to each of its neighbors. Meanwhile, a DOM is receptive to pulses from either or both of its neighbors. In local coincidence mode, only when this pulse arrives, will the DOM digitize, store, and subsequently transmit the time-stamped data to the surface.

2.3.2 Data compression

Since the local coincidence requirement eliminates a small fraction of real events [5], an alternative compression of all data including the noise hits has been developed. The waveforms captured by a single ATWD channel or the fADC are similar to a facsimile scan line. The original facsimile encoding standard [6] is based on "run-length" encoding followed by Huffman encoding [7] with a fixed, immutable, Huffman code. The adaptation of this idea to the digital waveform data has led us to a 4 step algorithm:

I: Gain channel selection: In most cases a waveform does not saturate or exceed the dynamic range of the high-gain channel of the ATWD. In these cases the low-gain channel information is redundant and discarded. However, should the high-

---

[7] The discrepancy of the pulse and hit noise rates is caused by the significant correlation of the noise - i.e. a single hit on average contains two pulses. The noise is mainly caused by radioactive decays in the glass of the pressure spheres and subsequent luminescence. The slow decay of the luminescence gives rise to the intrinsic correlation of the noise.

gain channel saturate this channel is discarded and instead the low gain channel data is preserved.

II: Zero suppression: The main purpose of this step is to reduce the entropy of the data set which makes the subsequently applied compression algorithms work more efficient. A threshold of a quarter of the average single photoelectron pulse height is applied to the data of the highest gain channel. This equivalent of a discriminator threshold is then subtracted from all sample values. Resulting negative values are set to zero.

III: Run-length encoding: This compression step replaces sequences ("runs") of consecutively repeated values with a single number prefixed by the length of the run. In the standard definition of run-length encoding the prefix count denotes occurrences and hence is always non-zero. In order to further gain efficiency for the compression in the subsequent *Huffman-lite* algorithm we choose to take the number of consecutive repetitions instead i.e. the prefix count is one less than with the standard definition and sample values occurring only once are prefixed with a zero. As a consequence about 50% of the resulting code are zeros.

IV: Huffman-lite encoding: Huffman coding simply uses shorter bit patterns as a replacement for more frequent values in the input stream than for rarely occurring values. We have reduced this concept to *Huffman-lite* in order to save computing resources. The bits used for zeros are minimized while we make no attempt to compress finite val-

ues. We convert a zero value "0" to a single bit '0'. In order to identify finite values these are preceded by a single high bit '1'.

For the STRING-18 configuration this compression reduces the data portion to 15 bytes per hit on average which is a factor of 40 down from the uncompressed data volume. In STRING-18 this compression algorithm is executed by the CPU in the DOM.

The STRING-18 data presented in Secs. 4 and 5 have been obtained using the compression to save bandwidth but without the local coincidence criterion to maximize the number of contributing DOMs and for straightforward comparison with the simulation based on the AMANDA detector and its trigger logic (see Sec. 5.3).

2.4 Surface DAQ

At the surface, the copper cables leading up from the DOMs are connected to custom communications cards (DOM-COM cards) in five industrial PCs with a Linux operating system. Aside from the DOMCOM cards all components of the surface DAQ are commercial hardware. The DOMCOM cards can be thought of as specialized serial ports for communicating with the DOMs with additional functions for powering on and off each DOM, and sending and receiving time calibration pulses. The five DOMCom PCs and a sixth, master control PC are connected by an Ethernet network. This network is then accessible via the South Pole station LAN and, at certain times during the

day, to the outside world via satellite connection. The principal task of the surface DAQ is to allow one to take control of and communicate with the DOMs in the ice for calibration and monitoring purposes and to collect data from the optical sensors.

FPGA logic in the DOMCOM boards provides input and output FIFOs connected to UARTs [8] in the DOMCOM boards. The UARTs in turn drive the communications circuits. Byte-wise communications of the DOMCOM interface to the DOMs is provided by a Linux kernel module device driver. By writing to and reading from FPGA registers mapped to port addresses the kernel driver allows Linux programs to communicate with the DOMs.

A suite of DAQ programs has been written to provide user interfaces for monitoring, control (HV settings, etc.) and data-taking purposes. Also, tools are available to reconfigure STRING-18 in many respects. Almost all of the components in the DOM can be reprogrammed after it is deployed in the ice. These include the DOM boot PROM, the code executed by its CPUs, and the FPGAs of both the DOM and the DOMCom card. For example, high speed communication and data compression in the DOM were implemented after the deployment and substantially improved the performance for physics data-taking.

---

[8] A UART or universal asynchronous receiver-transmitter translates between parallel bits of data and serial bits.
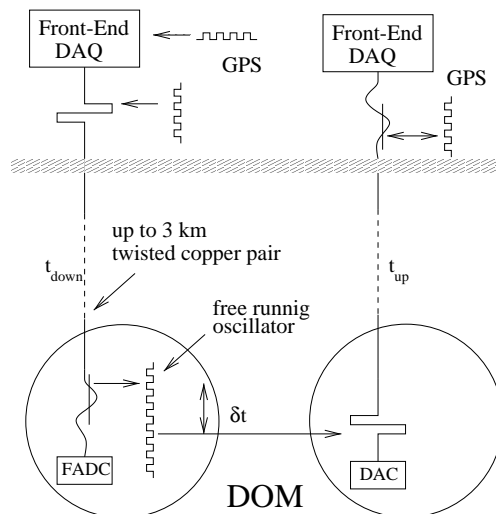
Figure 5. General concept of the Reciprocal Active Pulsing (RAP) method for time calibration.

3 Local to global time transformation

The (local) time stamp for a photon in a DOM must be converted to a global, i.e., array-wide time base, in order to be compared with hits in other DOMs. Correlation with events in nearby detectors, e.g. AMANDA and ICETOP, or much more distant detectors (satellites, other telescopes) requires converting the global time to universal time. Therefore, a critical requirement is the ability to calibrate the DOM local oscillator against a master clock at the surface.

3.1 Global time distribution

A GPS clock at the South Pole represents this master-clock for STRING-18. Its 10 MHz output is coupled to a special phase-locked loop on a clock distribution circuit. This PLL was set to give a frequency of 16.8 MHz in order

to match the frequency of the local oscillators in the DOMs. The 16.8 MHz signal is fed to each DOMCOM board in the five DOMCOM PCs where an additional PLL produces both 16.8 and 33.6 MHz phase-locked signals. The time jitter introduced by the PLL distribution system was measured to be less than 1 ns.

Figure 6. The timing pulse emitted by the DOMCOM card recorded over a 15 μs period as received by the DOM.

3.2 Reciprocal Active Pulsing

Timing pulses sent down the string to a DOM at known time intervals are used to determine relative frequency. In response to the calibration pulse received at the DOM, after a well-defined delay δt, a bipolar signal identical to the one sent down the string is sent back to the surface. With the pulses sent in both directions the offset of the two clocks at the surface and in the DOM are determined. The left part of Fig. 5 depicts the transmission of the timing pulse from the surface down to the DOM while the right hand side shows the transmission in the reverse direction with the same DOM and DOM-COM combination. It is important that the circuitry for generation and recording of the timing pulse be identical at the DOM and at the DOMCOM card and that the treatment is the same in both places. This way, the shapes of the pulses sent down and up are identical and can be analyzed in the same way to determine the time mark. This procedure yields an overall delay t_{rt} for the full round-trip. With the same signal treatment at the surface and in the DOM, one gets
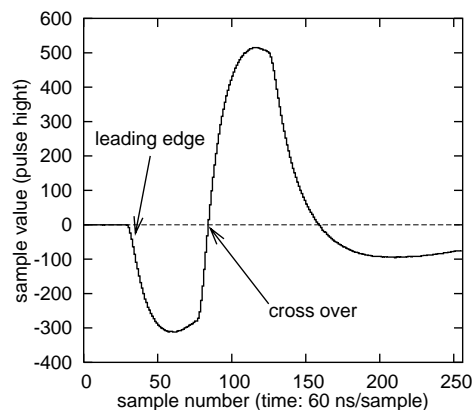
$$t_{up} = t_{down} = \frac{1}{2}\left(t_{rt} - \delta t\right) \ . \quad (1)$$

This calibration method is called Reciprocal Active Pulsing (RAP) [8]. It maps the local clock counter values in the DOM and the hit time-stamps to the global time.

Fig. 6 shows the shape of the timing pulse observed by the DOM at the end of a ∼2 km cable for a bipolar square-wave pulse injected by the DOMCOM card. The pulse displays the effect of cable attenuation and dispersion. The pulses are recorded at surface and at depth by fADCs whose sampling rates (16.8 MHz) are fixed by either the local oscillator in the DOM or the master clock on surface. The shapes of the pulses received by the DOMs and the DOMCOM cards are similar and indeed allow for the identical treatment.

Two methods were used to determine a reference time mark on the pulse:
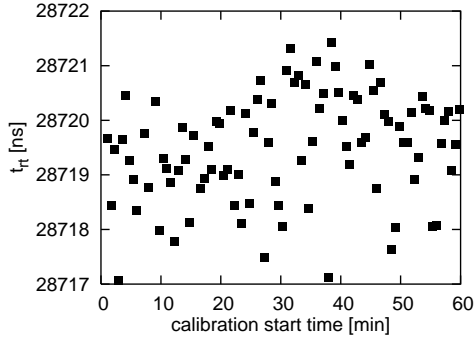
- The intersection of the baseline

13

Figure 7. Measured round-trip time t_{rt} from successive RAP calibrations for a DOM at 2 km depth.

voltage (linear fit) with the negative-going slope of the leading edge [9].

- The intersection of the crossover point (linear fit) with the extrapolated baseline.

We found that leading edge timing is least sensitive to variations in component values such as temperature variations after powering up. Crossover timing, however, gives better time resolution and has less jitter from one time calibration cycle to another. It was found that temperature drifts that show up in the cross over timing change the times t_{up} and t_{down} in identical amounts because the drifting electronic components affect both the up-going and the down-going pulses in the same way. This implies that the effect cancels for the calibration of the local time. Moreover, the observed drifts are very slow, less than 15 ns in 1 hour. Therefore, we have used the crossover timing to obtain the local to global time calibration. Fig. 7 shows the measured round-trip time t_{rt} (see Eq. (1)) over a period of one hour for a DOM at 2 km depth employing the cross over

----

[9] Tangent to the inflection point of a cubic function fit to the leading edge

timing. The jitter is 1.1 ns rms, which is a relative error of only $4 \cdot 10^{-5}$.

Performing these clock calibrations automatically every 10 seconds – as was done during data-taking with STRING-18 – consumes negligible bandwidth. We will demonstrate in Sec. 4.1 that this RAP method at this repetition rate provides a timing accuracy of better than 5 ns for the pulse times of a DOM.

4 Studies with optical beacons

To study the performance and uniformity of STRING-18 we have performed various dedicated data-taking runs operating the optical beacons of all available DOMs.

4.1 Timing accuracy

In order to determine the timing accuracy of the RAP calibration procedure described in Sec. 3 we have observed the light emitted by the LED beacon of one DOM by two neighboring DOMs. The beacon is set to a very bright output operation mode. For short distances the light front created at the beginning of a flash is to a good approximation unaffected by scattering in the ice as photons undergoing scattering fall behind the front. As long as there are enough photons as part of the light front, this front moves with the speed of light in the ice, c/n, where n is the refractive index. Hence, this light flash provides a reference time signal.

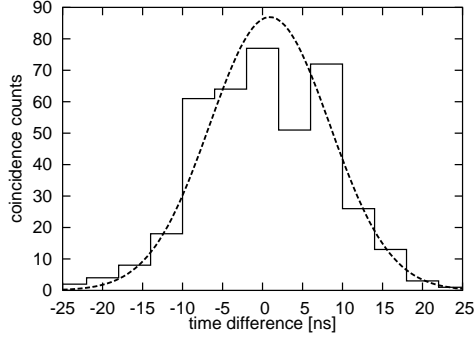Fig. 8 shows the measured time differ-

14

Figure 8. Relative timing accuracy of a pair of DOMs measured with a neighboring flashing beacon.

Figure 9. Attenuation of light from the optical beacon as a function of the distance from the source.

ence of the arrival times of this light front at both DOMs corrected for the propagation time of the light from one DOM to the other. One observes a distribution with a square root variance of 7.5 ns. The jitter includes effects of the PMT timing and the RAP procedure. Accordingly, this provides an upper limit for the timing accuracy of the RAP calibration process. Since both DOMs contribute to the variance of the observed time difference, the accuracy for an individual DOM with respect to the global surface time is about 5 ns.

4.2 Light propagation in the ice

We have studied the propagation of the LED light from the optical beacon (see Sec. 2.2.3) through the ice. From the beginning of AMANDA operations, it has been crucial to establish an understanding of the properties of the glacial ice at the South Pole [9]. Today the optical properties of the ice are mapped over the full relevant wavelength and depth range [10] using the analog optical modules.
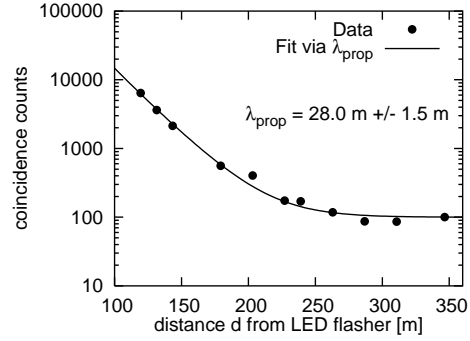
Using a configuration similar to the

one discussed in Sec. 4.1 we have used the flashing beacon in a DOM and observed the light in two other DOMs, one being the next neighbor to it. Here, the other observing DOM can be any other one along the string. Fig. 9 shows the coincidence counts of the two observing DOMs as a function of the distance d of the second observer DOM from a flasher at a depth of 1993 m below the ice surface. The first observing DOM as a neighbor to the beacon is close enough to observe every emitted flash. For DOMs further away photon counting in coincidence with the neighbor DOM is possible. The combined effect of scattering and absorption in the ice leads to a fall off of the light intensity I with an effective propagation length parameter λ_{prop}: $I(d) \propto \exp(-d/\lambda_{\mathrm{prop}})/d$ [11]. Random coincidences of the two observing DOMs due to the dark noise of the distant DOM [10] yields an additional offset c_2 independent of the distance. From fitting $c_1 \exp(-d/\lambda_{\mathrm{prop}})/d + c_2$ via c_1, c_2 and λ_{prop} we obtain $\lambda_{\mathrm{prop}} = 28.0 \pm 1.5\,\mathrm{m}$.

---

[10] The dark noise of the neighbor DOM can be neglected compared to the high flash rate.
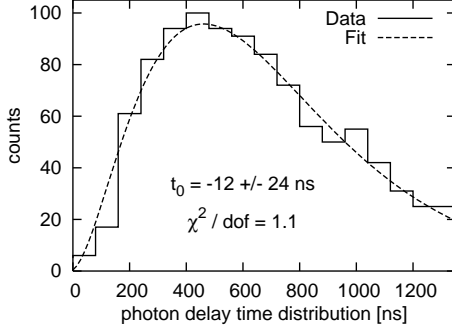
Figure 10. LED photon arrival time distribution due to scattering through 143 m of ice

With the described setup λ_{prop} represents a measurement of the average propagation length at depths between 1750 m and 1880 m. This is in excellent agreement with previous findings with the analog technology [10].

With the same setup we have also observed the arrival time distribution of the photons at the distant DOM (see Fig. 10). Here, the DOM next to the beacon provides the reference for the time of the flash. The time distribution is shifted to account for the time it takes light to traverse the ice without scattering from the beacon to the distant DOM (delay time distribution). The arrival time distribution for the DOM next to the beacon can be neglected as discussed in Sec. 4.1. Fitted to the data is a gamma distribution

$$f(t|t_0, \alpha, \beta) = (t - t_0)^{\alpha-1} \frac{\beta^\alpha e^{-\beta(t-t_0)}}{\Gamma(\alpha)} \tag{2}$$

for $t - t_0 > 0$ with a shape parameter $\alpha > 0$ and a scale parameter $\beta > 0$. Such a gamma function was found to describe the arrival time distributions reasonably well with scattering and

absorption in ice or water for the case of an isotropic, monochromatic and point-like light source [12,13]. The observed time distribution with the DOM follows this known behavior. As an additional parameter to the usual definition of a gamma distribution in Eq. (2) we have introduced t_0 to account for possible timing errors of the DOM. It turns out that t_0 is compatible with zero which is consistent with the results presented in Sec. 4.1.

5 Performance and analysis with atmospheric muons

Atmospheric muons provide a test beam for neutrino telescopes, as was demonstrated by AMANDA [14]. We will use it here to demonstrate the performance of STRING-18.

5.1 Down-going muons

The vast majority of the atmospheric muons that reach the detector travel at near the vacuum speed of light. The zenith angle distribution is peaked in the downward direction. We have compared the coincidence hit times of the DOMs with the hypothesis of a straight down going muon, i.e. we have subtracted the time it takes the muon from the upper DOM to the lower one from the hit time differences. Fig. 11 shows the distribution of these time differences under the condition that at least 4 DOMs of the string registered the event. On the left of Fig. 11 we show the distribution of time differences of a particular pair of DOMs. The two
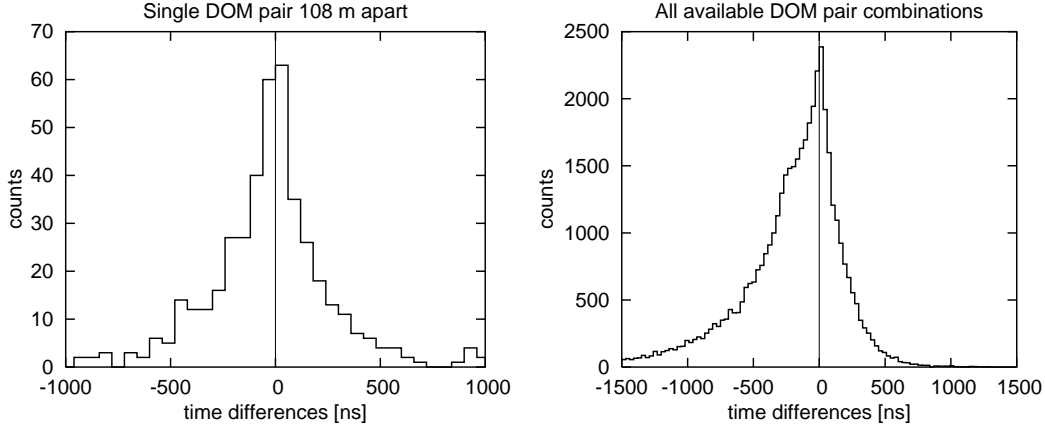
16

Figure 11. Time differences between pairs of DOMs corrected for the down-going muon hypothesis. Left: single DOM pair 108 m apart, right: all available DOM pair combinations accumulated.

DOMs are 108 m apart. The right hand side of Fig. 11 shows an accumulation of these diagrams for all available pairs of DOMs. With the hypothesis of a straight down-going muon, the peak count should be at zero. The exact location of the peak at zero to within a nanosecond, which can be seen by examining the peak region in more detail than shown, is another evidence for the accurate timing and the proper functioning of the RAP calibration method.

The asymmetry of the tails of the distribution towards negative time differences is a consequence of not quite straight down-going muons. For small zenith angles of the muon track the Cherenkov light that reaches the DOMs does indeed cause hit times that proceed from top to the bottom of the string that appear faster than the vacuum speed of light. A muon track at zenith angle $90° − \theta_{\check{C}}$ ($\theta_{\check{C}}$ is the Cherenkov light emission angle) that intersects the string will cause all DOMs located above the intersection point to light up at once (neglecting scattering in the ice). By shifting the

time differences with the hypothesis of a straight down going muon one obtains these negative time differences. We will see in Sec. 5.2 that these deviations can indeed be used to reconstruct the zenith angle of the muon track.

Fig. 12 shows the mean time differences of all available pairs of DOMs as a function of the separation of the DOMs. For this plot the time differences were not shifted for the down-going muon hypothesis and we require that no fewer than 6 DOMs have "seen" the muon. A linear fit to the data shows a slope compatible with straight down-going muons traveling at the speed of light. The intercept of the fit at $−2.3\,\mathrm{ns} \pm 7.2\,\mathrm{ns}$ is another indication that the local to global time transformation works.

5.2 Zenith angle reconstruction

In the absence of scattering and absorption in the Cherenkov medium the arrival time of the Cherenkov light
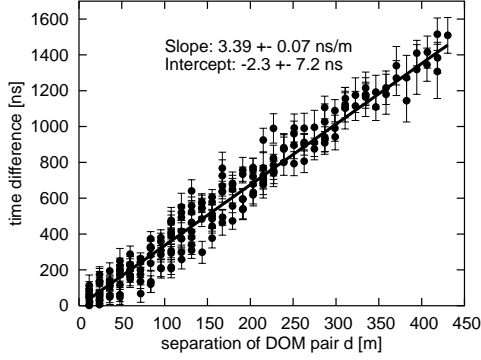
17

Figure 12. Time differences between all available pair combinations of DOMs as a function of the separation.

from the muon at the string takes the simple analytic form of a hyperbola as a function of the depth z along the string [15] [11]:

$$t = t_0 + \frac{1}{c}\left\{(z - z_0)\cos\theta + \sqrt{(n^2 - 1)[d^2 + (z - z_0)^2\sin^2\theta]}\right\} \tag{3}$$

Here, d is the minimum distance between the string and the muon track; θ is the zenith angle of the muon; t_0 and z_0 are the time and the depth at which this closest approach of the muon occurs. Since t_0 is not directly related to the observable hit times of the DOMs we replace it by $t_{first} = t_0 + d\sqrt{n^2 - 1}/c$ which is an estimate for the time when the Cherenkov light from the point (t_0, z_0) reaches the string [12].

The 4 parameters t_{first}, z_0, d and θ are to be fitted to the data. We have used the *GNU Scientific Library* [16] to perform this nonlinear multiparameter fit. Computing the Jacobian matrix from explicit derivatives greatly improves the numerical stability and provides fit results practically independent of the initial guess of the parameters as long as they are chosen within a physically reasonable region – e.g. z_0 in between the actually hit DOMs. To calculate the derivatives we have used the computer algebra system *Maxima* [17]. For the initial guess we have used $d = 0$ and $\theta = 90°$. The guess for z_0 was computed as the average z of all hit DOMs weighted with the pulse charges. The initial value of t_0 was set to the hit time of the DOM next to z_0. Eq. (3) holds for the idealized situation without scattering and absorption in the medium. The ice at the South Pole however shows scattering and absorption. By integrating the gamma function mentioned in Sec. 4.2 with the empirical parameters successfully used in AMANDA [13] one obtains that the mean speed of propagation of the light is about 11 ns/m in contrast to the expectation of about 5 ns/m based on the refractive index of ice of $n = 1.32$. To account for that we have replaced n in Eq. (3) by $n_{eff} \simeq 3.16$. Note that the effective opening angle of the light cone [13] of the produced Cherenkov light is reduced as well. This is why a simple replacement of n by n_{eff} in Eq. (3) is consistent.

---

[11] We have to caution that the approximation presented as Eq. (5) in Ref. [15] is wrong for all $z - z_0 < 0$. We have not used this approximation but the exact description of the hyperbola with our Eq. (3).

[12] This of course disregards the initial ori-

---

entation of the Cherenkov light. Scattering in the ice however largely voids this feature.

[13] The initial emission angle of the Cherenkov light is unaffected, of course.
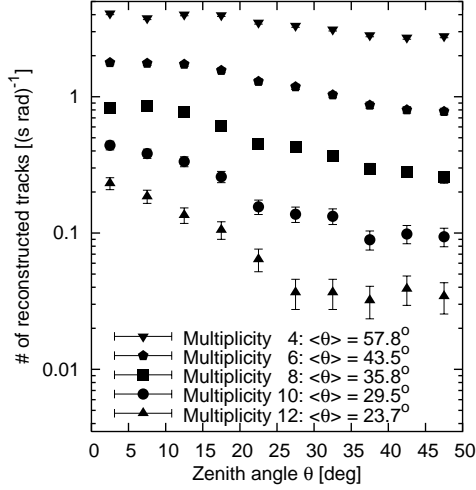
Figure 13. Reconstructed zenith angle distribution with STRING-18 for several multiplicity conditions

Fig. 13 shows the zenith angle distribution as reconstructed with this method applied to STRING-18. Here, a zenith angle of zero denotes a straight down-going muon. One observes that the angular distribution falls off faster with higher required multiplicities of the number of hit DOMs. This is an effect related to the acceptance changing with increasing multiplicity. Due to the absorption of the Cherenkov light in the ice, only close by vertical tracks have a chance to be seen by all DOMs. However close a track might be, even when intersecting with the string, a horizontal track has a very low chance to light up more than only a handful of DOMs.

5.3 Comparison with simulation

We have compared the observed rates of muon tracks with a detailed simulation in order to verify that STRING-18 indeed performs with a homogeneous efficiency. The acceptance for

muon tracks agrees with the expectations based on the parameters of the whole light collection process i.e. the optical coupling of the ice to the pressure sphere, the glass and gel transmission and the quantum efficiency of the PMT. The simulation is based on the air shower generator CORSIKA [18], a program package for muon propagation through matter MMC [19,20] and the AMANDA detector simulation program AMASIM [21]. This simulation for the full AMANDA detector was restricted to the STRING-18 geometry.

Besides generating hit times for the DOMs the simulation also provides the zenith angle of the generated muon tracks. By applying the reconstruction method of Sec. 5.2 to the simulated hits one can study the performance of the reconstruction algorithm. It turns out that the distribution of the deviation of the reconstructed zenith angle from the generated muon track angle roughly follows an exponential behavior $\propto \exp(-\Delta\theta/b)$ with $b \simeq 22°$. This corresponds to a median error of $15°$.

This reconstruction technique is of course inferior to the full AMANDA reconstruction [13]; the main limitation here stems from the reduced geometry of a single string versus an array of optical modules. Also the chosen approach to reconstruction is much simpler. It was not the primary aim of this analysis to provide an optimized reconstruction method. However, the error of the reconstruction method is small enough to calculate angular distributions that show the characteristic features.
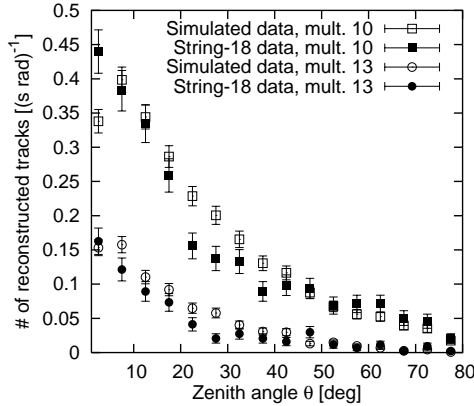
Fig. 14 shows a comparison of muon

Figure 14. Muon tracks reconstructed with STRING-18 data and with simulated data for two multiplicity conditions.

tracks reconstructed with STRING-18 data to tracks reconstructed with simulated data. Note that the distributions have *not* been scaled with respect to absolute numbers. The agreement found both in shape and in absolute rates is excellent and shows that efficiencies and timings are well under control in STRING-18.

6 Conclusion

STRING-18 is established as proof of concept for the ICECUBE array. The all-digital technology with pulse digitization already at the PMT inside the optical module, digital data transmission to the surface and automated time calibration was shown to be fully functional including the benchmark observation of atmospheric muons.

Acknowledgements

References

[1] AMANDA Collaboration, E. Andrés et al., Nature 410 (2001) 441.

[2] IceCube Collaboration, IceCube Preliminary Design Document, 2001, http://icecube.wisc.edu.

[3] IceCube, J. Ahrens et al., Astropart. Phys. 20 (2004) 507, astro-ph/0305196.

[4] S.A. Kleinfelder, IEEE Trans. Nucl. Sci. 50 (2003) 955.

[5] J. Jacobsen and R.G. Stokstad, Consequences of a local coincidence

for a large array in ice, 1998, LBNL INPA Internal Report, LBNL-41476.

[6] R. Hunter and A. Robinson, Proceedings of the IEEE 68 (1980) 854.

[7] D.A. Huffman, Proceedings of the Institute of Radio Engineers 40 (1952) 1098.

[8] R.G. Stokstad et al., LBNL preprint LBNL-43200 (1998).

[9] AMANDA Collaboration, P. Askebjer et al., Geophys. Res. Lett. 24 (1997) 1355.

[10] AMANDA Collaboration, K. Woschnagg et al., Nucl. Phys. Proc. Suppl. 143 (2005) 343, astro-ph/0409423.

[11] P. Askebjer et al., Appl. Opt. 36 (1997).

[12] D. Pandel, 1996, Diploma thesis, Humboldt University, Berlin.

[13] AMANDA Collaboration, J. Ahrens et al., Nucl. Instrum. Meth. A524 (2004) 169, astro-ph/0407044.

[14] AMANDA Collaboration, E. Andres et al., Astropart. Phys. 13 (2000) 1.

[15] ANTARES Collaboration, E. Carmona, (2001), ICRC 2001, Hamburg.

[16] The GNU Project, GSL - GNU Scientific Library, http://www.gnu.org/software/gsl/.

[17] Maxima - a sophisticated computer algebra system, http://maxima.sourceforge.net/.

[18] J. Knapp and D. Heck, Nachr. Forsch. zentr. Karlsruhe 30 (1998) 27.

[19] D. Chirkin, Cosmic Ray Energy Spectrum Measurement with the Antarctic Muon and Neutrino Detector Array (AMANDA), PhD thesis, UC Berkeley, 2003.

[20] D. Chirkin and W. Rhode, (2004), hep-ph/0407075.

[21] S. Hundertmark, AMASIM neutrino detector simulation program, Prepared for International Workshop on Simulations and Analysis Methods for Large Neutrino Telescopes, Zeuthen, Germany, 6-9 Jul 1998.